RSC Advances

ROYAL SOCIETY OF CHEMISTRY

www.rsc.org/advances

Atomic approach to the optimized compositions of Ni-Nb-Ti glassy alloys with large glass-forming ability

Y. Li , J. H. Li*, J. B. Liu , B. X. Liu

Key Laboratory of Advanced Materials (MOE), School of Materials Science and Engineering, Tsinghua University, Beijing 100084, China

ABSTRACT

In the present study, we first constructed a long range empirical potential for ternary Ni-Nb-Ti system consisting of *fcc*, *bcc* and *hcp* metals, and then employed the verified potential in atomic simulations to study the formation of Ni-Nb-Ti glassy alloys. Atomic simulations derived a pentagon composition region of Ni-Nb-Ti system, within which glassy alloys are inclined to form. Furthermore, the driving force for the transformation from a crystalline solid solution to glassy alloy could be correlated to the glass-forming ability (GFA) of a particular alloy. The GFA of ternary Ni-Nb-Ti alloys with various compositions were assessed on the basis of atomic simulation results, obtaining an optimized composition region, within which the alloys possess larger GFA, as well as an optimum composition with the largest GFA. The optimum alloy is expected to be the most stable or the size of obtainable glass may be the largest in ternary Ni-Nb-Ti system. The optimized composition region and optimum composition could provide guidance to design the compositions of Ni-Nb-Ti metallic glasses.

Keywords: metallic glass, GFA, optimized compositions, atomic simulation

* Corresponding author: lijiahao@mail.tsinghua.edu.cn

1. Introduction

Due to the remarkable properties, such as high elastic modulus, good corrosion resistance and high strength, bulk glassy alloys (BMG) are considered to have broad prospect in industrial applications.[1-6] Among the BMG, lots of Ni-based BMG were produced by copper mold casting, which reveals good ductility.[7-11] As representative Ni-based BMG, Ni-Nb-Ti metallic glasses exhibit high compressive fracture strength of over 3 GPa and high thermal stability.[12,13] Especially, the Ni-Nb-Ti alloys have been focused on the intriguing properties such as considerable shape memory effect and pseudo-elasticity and hence could be used as functional materials for micro-electromechanical system devices.[14,15] These findings stimulated us to study the formation of ternary Ni-Nb-Ti glassy alloys, which would facilitate our understanding on the underlying glass formation mechanism.

Researchers in the area of BMG focus on searching for the bulk metallic glass with large glass-forming ability (GFA)[16,17]. To search for desired metallic glass formers, the empirical rules, such as deep eutectic criteria[18], atomic size difference rule[19] and Inoue's rules[20], haven been put forward, some related issues are not solved yet[21]. As a consequence, it is necessary and significant to develop a capable model to predict the GFA of glassy alloys so as to design the optimized glassy alloys with large GFA.[21-23] In a physical perspective, GFA can be thought as the intrinsical property of an alloy and is predominated by the interactions of constituent atoms. Consequently, one is able to utilize an atomic approach to derive the GFA from the potential that represents the prime atomic interaction.

To give a comprehensive consideration of the formation of ternary Ni-Nb-Ti glassy alloys, the glass formation region (GFR) is first taken into account. The GFR indicates the alloy composition region of the system within which glassy alloys could be fabricated by certain production techniques.[24] Once the GFR is determined, the GFA of glassy alloys with various compositions within the GFR could be evaluated through some simulation methods.[23,25]

Considering the preparation process of glassy alloys, glass formation is thought as the suppression or failure of crystallization, or the result of a stabilized state inherited from liquids below the glass transition temperature. As the glassy alloys always undergo a nonequilibrium process, owing to the kinetic restrictions, intermetallics frequently with complex structures are suppressed to nucleate or grow, leading to the formation of either simple structured crystals or disordered phases.[24] It can be deduced that the major competing phase against glassy alloy is the crystalline solid solution which has simple structures, i.e., body-centered cubic (*bcc*), face-centered cubic (*fcc*), or hexagonal close packed (*hcp*), considering the suppressing of the formation of intermetallics.[26] In fact, the formation enthalpy difference between amorphous and crystalline alloy is approximately considered as the driving force for amorphization of a solid solution, which can correlate to the GFA of a particular alloy.[25] It is deduced that the larger the driving force, the more easily glassy alloy can form, or the less the critical cooling rate, or the larger the critical casting size. In consequence, the GFA could be evaluated based on the magnitude of the driving force for metallic glass formation.

In literature, atomic simulations usually focus on the formation and structure of those metallic glasses whose constituent metals are two different structures, i.e. *fcc-bcc*, *fcc-hcp*, or *bcc-hcp*.[25,27-29] In the present research, a long range realistic empirical potential was built for ternary Ni-Nb-Ti metallic system with three different constituent structures (*fcc*, *bcc*, and *hcp*). After that, the potential was utilized in atomic simulations to study the formation of Ni-Nb-Ti glassy alloys. According to atomic simulation results, the GFA of Ni-Nb-Ti alloys were estimated and the optimized compositions with large GFA were derived.

2. Ni-Nb-Ti interatomic potential

Lately, Dai and Li put forward a long range empirical potential (LREP) that can be applied in transition metallic systems comprising *bcc*, *fcc*, or *hcp* metals.[30-32] The LREP is utilized in the present research due to its efficiency and validity in expressing the atomic interactions of transition metallic systems. Therefore, the LREP energy E_i of atom i can be computed by the equations as follows:

$$E_i = \frac{1}{2}\sum_{j\neq i} V(r_{ij}) - \sqrt{\sum_{j\neq i}\varphi(r_{ij})}\,, \tag{1}$$

$$V(r_{ij}) = (r_{c1} - r_{ij})^m (c_0 + c_1 r_{ij} + c_2 r_{ij}^2 + c_3 r_{ij}^3 + c_4 r_{ij}^4), \qquad 0 < r_{ij} \le r_{c1}\,, \tag{2}$$

$$\phi(r_{ij}) = \alpha(r_{c2} - r_{ij})^n, \qquad 0 < r_{ij} \le r_{c2}\,, \tag{3}$$

m, n, α, and c_i are the LREP parameters to be determined in fitting procedure. r_{c1} and r_{c2} are the cutoff distance of the LREP. The details on Equations (1)-(3) can be referred to Ref. 28. From Equations (1)-(3), it can be discovered that the LREP energy converges to zero continuously and smoothly at the cutoff distances, therefore

obviating the energy leaps and force leaps as well as the related unphysical behaviors during atomic simulations. Compared with other potentials such as MEAM potential proposed by Baskes[33], the LREP greatly simplifies the computation of interactions without considering the angular factors, which is reasonable in transition metallic systems while the metallic bonding exhibits a non-directional feature. Applying the LREP rather than MEAM, the time cost of atomic simulation can reduce to a fraction between one fifth and one tenth, indicating a much faster running speed. The LREP can also be applied in metals with different structures (*fcc*, *bcc*, and *hcp*), while the MEAM meets some problems applying in *bcc* metals.

In the Ni-Nb-Ti system, LREP parameters for Ni-Ni, Nb-Nb, Ti-Ti, Ni-Nb, Ni-Ti, and Nb-Ti interactions are requisite The Ni-Ni and Nb-Nb LREP parameters have been given in Ref. 29 and were directly employed in present work. Therefore, it's just required to determine the Ti-Ti LREP parameters by fitting to the reference physical properties (lattice constants, cohesive energies, and elastic modulus) of *hcp*-Ti in experiment. To fit Ni-Nb, Ni-Ti, and Nb-Ti cross LREP, intermetallics with different compositions and atomic configurations are utilized to make sure that the obtained LREP is good enough to express the atomic interactions in different atomic configurations. Without enough experiment data of Ni-Nb-Ti intermetallics i, especially the binary Nb-Ti compounds, *ab initio* calculations based on density functional theory (DFT) were conducted using CASTEP.[34,35] In the *ab initio* calculations, nonlocal ultrasoft pseudopotentials were employed to represent the electron-ion interaction. The energy cutoff for plane-wave basis was 700 eV and the

Brillouin zones of various structures were sampled with the same *k*-points spacing, which approximately equals to a mesh of 20 × 20 × 20 for a *bcc* unit cell. The exchange-correlation functional was constructed based on the generalized gradient approximation of Perdew and Wang (PW91)[36]. Those setting parameters were verified to make sure the calculation satisfied the requirements for energy convergence and precision. At first, geometry optimization was conducted to acquire the lattice constants and enthalpies of the intermetallics. The elastic moduli of the optimized intermetallics were consequently computed. The cohesive energies of the intermetallics are able to be obtained from the enthalpies. The formation heats and cohesive energies can be deduced from each other. For convenience, only the cohesive energies were listed in this article. The constructed Ni-Nb-Ti LREP parameters are presented in Table 1. The physical properties (lattice constants, cohesive energies, elastic moduli, and bulk modulus) of *hcp*-Ti obtained from LREP and experiment[37-39] are shown in Table 2. The physical properties of intermetallics in binary Ni-Nb, Ni-Ti, and Nb-Ti systems obtained from the LREP and experiment[28,40] (or *ab initio* calculations) are exhibited in Tables 3, 4, and 5. It can be seen that the physical properties obtained from LREP and experiment (or *ab initio* calculations) exhibit consistency, proving the validity of the constructed LREP..

It is significant to assess the reliability of the LREP in a non-equilibrium environment by comparing the equation of state (EOS) deduced from the LREP with Rose Equation (RE)[41]. The EOS for the metals and intermetallics obtained from the LREP and RE are displayed in supplementary Figures S1 and S2. It can be seen that

the major part of energy curve obtained from the LREP exhibit good consistency with RE in the overall variation range. Though it can be seen deviations between the blue and red dot curves in Figure S2, the deviations emerge in the vicinity of $a = 1.5a_0$ which are so far from equilibrium that it hardly take place in actual situation. Therefore, it is considered that the Ni-Nb-Ti LREP are able to describe the atomic interactions in a non-equilibrium environment reasonably.

3. Atomic simulation methods

As discussed in Section 1, the nucleation and growth of intermetallic compounds were suppressed due to kinetic restrictions, and the intermetallics were hardly observed during the short time of simulation process (several nanoseconds). Consequently, the prime competing phase against amorphous alloy is the *fcc*, *bcc*, or *hcp* solid solution, especially when the alloy composition is located close to the pure metals. Therefore, one can translated the issue involved with the GFR of Ni-Nb-Ti system into that of comparing the energy stability of a crystalline solid solution with its corresponding amorphous state (glassy alloy). The solid solution model has been successfully applied in several ternary metallic systems such as Cu-Zr-Al and Ni-Zr-Al systems to investigate the formation of ternary glassy alloys.[23]

Applying Ni-Nb-Ti LREP, a sequence of molecular dynamics (MD) simulations were first performed employing Large-scale Atomic/Molecular Massively Parallel Simulator (lammps) packages[42] to investigate the GFR of Ni-Nb-Ti system. During the atomic simulations, *fcc*, *bcc* and *hcp* solid solutions were built considering the fact

that the stable structures of Ni, Nb, and Ti metals at the simulation temperature (300K) are *fcc*, *bcc*, and *hcp*, respectively. The structure of a solid solution was determined according to the major component of the alloy. *Fcc* solid solution comprises 2916 ($9\times9\times9\times4$) atoms, *bcc* solid solution comprises 3456 ($12\times12\times12\times2$) atoms, and *hcp* solid solution comprises 3328 ($13\times8\times8\times4$) atoms. For both *fcc* and *bcc* solid solutions, *x*, *y*, and *z* axes are parallel to the [100], [010], and [001] crystalline orientations, respectively. In *hcp* solid solutions, *x*, *y*, and *z* axes are parallel to the $[11\bar{2}0]$, $[\bar{1}100]$, [0001] crystalline orientations, respectively. Periodic boundary conditions were set in *x*, *y*, and *z* axes. In constructing the solid solutions, the solvent atoms were replaced stochastically by a setting number of solute atoms to acquire an expected concentration. MD simulation was performed in the framework of isothermal-isobaric ensemble with a time step of 5 femtoseconds. The simulation proceeded at 300 K and 0 Pa for 1 million time steps (5 nanoseconds) to achieve a stable state.

In addition to MD simulation, a sequence of Monte Carlo (MC) simulations were conducted to calculate the formation enthalpy of solid solutions[43]. The initial solid solutions were constructed analog to that conducted in MD simulation. Periodic boundary conditions were applied in the three axes. MC simulations proceeded at 300K and 0 Pa under the isothermal-isobaric ensemble[44]. During the relaxation period of solid solutions, the fractional coordinates of atoms in the simulation box were fixed, while the simulation box either expanded or contracted. In another word, the atoms can't move relative to the simulation box but move along with the simulation box. In this way, the MC simulation proceeded in the box deformation mode and the solid

solutions can achieve the state with the minimum energy by adjusting the lattice constants while the crystallographic symmetry remained invariable. The relaxation period during for solid solutions towards the minimum energy state lasted for thousands of steps. The stable solid solutions preserved the initial structure with lattice constant which was usually different from the initial settings.

To investigate the structural variation in detail, the pair correlation functions[45] and atomic projections were employed to analyze the atomic coordinates based on the atomic simulations. The total pair correlation functions $g(r)$ and the partial pair correlation functions of atoms A and B $g_{AB}(r)$ can be computed by

$$g(r) = \frac{V}{N^2 \cdot 4\pi r^2 \Delta r} \sum_{i}^{N} \sum_{j}^{N} \delta(r - r_{ij}), \quad (4)$$

and

$$g_{AB}(r) = \frac{V}{N_A N_B \cdot 4\pi r^2 \Delta r} \sum_{i \subset A}^{N_A} \sum_{j \subset B}^{N_B} \delta(r - r_{ij}), \quad (5)$$

The details on the equations (4) and (5) can be referred in Ref 45. The $g(r)$ presents the average radial arrangements of neighboring atoms around a particular atom, which can reflect the long range order of the atomic configurations. For ordered strucutres such as crystalline solids, the $g(r)$ shows a sequence of peaks, while for disordered structures such as liquids or amorphous solids, the $g(r)$ reveals a sequence of oscillating peaks which decays and approaches one at long distance. In consequence, the $g(r)$ can be used to characterize the crystalline or amorphous atomic configurations of the simulated alloys.

Except pair correlation functions, Voronoi tessellation[46] were adopted to inspect the structure variation of the simulated atoms. The tiny facets of Voronoi polyhedra (area lower than 1% of the average area) were excluded in the statics of coordination number and Voronoi index. Based on Voronoi tessellation, the coordination number and Voronoi polyhedra can be analyzed, which uncovers the neighboring atomic information within a given cutoff radius. The variation of neighboring atomic arrangements contributes to the distinction between crystalline and amorphous atomic configurations, which assists us to characterize the atomic structure variation.

4. Metallic glass formation in the Ni-Nb-Ti system

To verify the reliability of the simulated glass formation revealed by MD simulations, the atomic configurations of the simulated metallic glasses were compared with experimental data. Considering the lack of experimental data on the atomic structure of ternary Ni-Nb-Ti metallic glass, the $g_{AB}(r)$ of the simulated $Ni_{62}Nb_{38}$ amorphous alloy and $Ni_{40}Ti_{60}$ alloy were compared with experimental data,[47,48] as shown in Figure 1. From Figure 1(a), one can see the nearest-neighbor atomic distances of $r_{Ni\text{-}Ni}$, $r_{Ni\text{-}Nb}$ and $r_{Nb\text{-}Nb}$ of $Ni_{62}Nb_{38}$ metallic glass are 2.40 Å, 2.60 Å, and 2.70 Å, respectively, in agreement with the experiment values[47] ($r_{Ni\text{-}Ni}$ = 2.48 Å, $r_{Ni\text{-}Nb}$ = 2.63 Å, and $r_{Nb\text{-}Nb}$ = 3.05 Å) for $Ni_{62}Nb_{38}$ amorphous alloy from neutron diffraction at room temperature. Moreover, it can be found from Figure 1(b) that $r_{Ni\text{-}Ni}$, $r_{Ni\text{-}Ti}$ and $r_{Ti\text{-}Ti}$ of $Ni_{40}Ti_{60}$ metallic glass are 2.50 Å, 2.55 Å, and 2.80 Å, respectively, conforming with the experiment data[48] ($r_{Ni\text{-}Ni}$ = 2.63 Å, $r_{Ni\text{-}Ti}$ = 2.60 Å, and $r_{Ti\text{-}Ti}$ = 3.01

Å) from X-ray and neutron diffractions. Although there are deviations between the nearest-neighbor atomic distances of the simulated alloy and those from diffraction data, the outlines of the $g_{AB}(r)$ are similar, which revealed similar disordered features of the metallic glasses. According to the comparison above, the structures of simulated $Ni_{62}Nb_{38}$ and $Ni_{40}Ti_{60}$ alloys is thought to be analogous to those of real alloys, indicating that the formation of Ni-Nb-Ti metallic glass revealed by MD simulations is valid and believable.

To provide an overall and comprehensive understanding on the metallic glass formation in ternary Ni-Nb-Ti system, the $Ni_xNb_yTi_{100-x-y}$ (x, y vary with a seperation of 5%) solid solution were first created within all the composition region, and subsequently, MD simulations were run on the basis of the realistic LREP in Section 2. Viewing the atomic simulation results, the atomic configurations of the Ni-Nb-Ti alloys display two structure types, that is an ordered crystalline structure (OCS) and a disordered amorphous structure (DAS). To illustrate both the typical atomic structures, $Ni_{15}Nb_{45}Ti_{40}$ and $Ni_{25}Nb_{40}Ti_{35}$ alloys served as an example. The pair correlation functions $g(r)$ and atomic projections for both crystalline and amorphous structures are presented in Figure 2. It can be found that the $g(r)$ of the $Ni_{15}Nb_{45}Ti_{40}$ alloy reveals typical *bcc* crystalline peaks in Figure 2(a), which is testified by the ordered atomic projections of *bcc* crystals exhibited in Figure 2(b). Figures 2(a) and 2(d) indicates that the $Ni_{15}Nb_{45}Ti_{40}$ alloy has maintained the initial ordered crystalline structure. The $g(r)$ of the $Ni_{25}Nb_{40}Ti_{35}$ alloy in Figure 2(c) exhibits a typical amorphous $g(r)$, which implies a structure feature of long range disorder. The

amorphous structure is manifested by the disordered atomic projections in Figure 2(d), which suggests that the initial crystalline structure of $Ni_{25}Nb_{40}Ti_{35}$ alloy has been destroyed and transformed to an amorphous structure.

To further inspect the atomic configurations of the $Ni_{15}Nb_{45}Ti_{40}$ and $Ni_{25}Nb_{40}Ti_{35}$ alloys, the distributions of coordinate number (CN) and Voronoi volume as well as populations of the Voronoi polyhedra are presented in Figures 3 and 4. Figure 3(a) shows that although the prime CNs of the $Ni_{15}Nb_{45}Ti_{40}$ and $Ni_{25}Nb_{40}Ti_{35}$ alloys are both 13, 14 and 15, the fraction of CN = 14 in the $Ni_{15}Nb_{45}Ti_{40}$ alloy is close to 60% and much more than the factions of CN = 13 or 15, implying a typical *bcc* crystal feature and an obvious distinction from the lower fraction of CN = 14 in the $Ni_{25}Nb_{40}Ti_{35}$ alloy. In Figure 3(b), a sharp bulge emerge on the curve of voronoi volume of $Ni_{15}Nb_{45}Ti_{40}$ alloy rather than that of $Ni_{25}Nb_{40}Ti_{35}$ alloy. Except for the distribution of CN and voronoi volume, Voronoi index of the most common Voronoi polyhedra are exhibited in Figure 4. From Figure 4(a), one can see that the most common Voronoi polyhedra of $Ni_{15}Nb_{45}Ti_{40}$ alloy are (0, 6, 0, 8) and (0, 4, 4, 6), which can be considered as the *bcc* crystal structure or distorted *bcc* structure. It can be seen from Figure 4(b) that the most common Voronoi polyhedra of $Ni_{25}Nb_{40}Ti_{35}$ alloy are (0, 3, 6, 4) and (0, 2, 8, 4), implying the main coordination numbers are 13 and 14. However, it is noted that the fractions of the Voronoi polyhedra with different Voronoi index are very close and all lower than 5%, which indicates that the crystalline structure of $Ni_{25}Nb_{40}Ti_{35}$ alloy was destroyed and the atomic structure has evolved to an amorphous glass. According to the above Voronoi tessellation analysis,

it is deduced that $Ni_{15}Nb_{45}Ti_{40}$ alloy has preserved the initial *bcc* structure, while $Ni_{25}Nb_{40}Ti_{35}$ alloy has transformed to an amorphous alloy. Based on the structure analysis above, the transformation from crystalline solid solutions to amorphous glasses reveals that the atomic process of glass formation is the crystalline lattice destabilization of solid solutions in circumstances that the solute concentration surpasses the threshold of solid solubility.

Considering the atomic configurations derived from atomic simulations, all the simulated $Ni_xNb_yTi_{100-x-y}$ alloys were sorted into the OCS and DAS, and consequently, plotted the Ni-Nb-Ti glass formation composition region in Figure 5. It can be seen from Figure 5 that two OCS-ACS boundaries (polyline ABC and line DE) partition all the composition region into three areas. The two lines are considered as solid solubility boundaries as well. One can find from Figure 5 that when the composition is located over line DE towards the Ni vertex, or over polyline ABC towards the Nb-Ti side, the Ni-Nb-Ti alloy inclines to maintain its initial crystalline structure (OCS). In consequence, the two areas are defined as the crystalline regions. When the alloy composition is located inside the shaded zone surrounded by the polyline ABC and line DE (red lines) and the triangle edges, the crystalline solid solution becomes destabilized and collapses, transforming into a disordered structure (DAS). The shaded zone is identified as the amorphous region. As a consequence, we define the shaded pentagon region (amorphous region) as the GFR of Ni-Nb-Ti system, within which the metallic glasses are inclined to form energetically.

It is necessary and significant to make a comparison between the derived Ni-Nb-Ti GFR with experimental observations. One notes that plenty of metallic glasses were obtained in binary Ni-Nb, Ni-Ti and ternary Ni-Nb-Ti systems by various production techniques such as ion beam mixing (IBM)[49], rapid solidification (RS)[12,50,51], combinatorial arc plasma deposition (CAPD)[13] and mechanical alloying (MA)[52]. The compositions of glassy alloys synthesized by the above techniques were flagged by colorful symbols as indicated in Figure 5. Figure 5 indicates that the GFR of binary Ni-Nb system is acquired from the IBM data as 15-80 at.% Nb, while the RS results reveal the GFR of 30-60 at.% Nb. Both the GFR obtained from experiments are either close to or within the GFR of 20-75 at.% Nb derived from atomic simulations, implying that the experimental observations and the atomic simulations of Ni-Nb alloys are in good consistency, considering the 5 at.% composition error. The GFR of 28-72 at.% Ti in Ni-Ti system achieved through MA was compared with that of 20-80 at.% Ti predicted in Figure 5, showing good accordance. The Ni-Nb-Ti metallic glasses were produced through CAPD within the composition region of 25-80 at.% Ni, 0-70 at.% Nb, and 0-75 at.% Ti[13], which is very close to the predicted GFR. In brief, all the experimental results are located in the predicted GFR, indicating the predicted GFR in present research are realistic and reliable.

It's interesting to compare the predicted GFR of Ni-Nb-Ti system with those predicted GFR of Ni-Nb-Mo[29] and Ni-Nb-Zr[53] systems as well. It is found the GFR of Ni-Nb-Zr reveals the largest glass formation composition region covering the Nb-Zr

side, and the GFR of Ni-Nb-Ti indicates a relative smaller glass formation composition region, while the GFR of Ni-Nb-Mo exhibits the smallest glass formation composition region. The GFR of the three metallic systems signifies that the Zr, Ti and Mo elements all contributes to improving the GFR of the Ni-Nb system while the alloying effect of three elements on the Ni-Nb metallic glasses show some distinctions. The comparison also indicate that the GFR of metallic systems with three different metal structures (Ni-Nb-Ti and Ni-Nb-Zr) indicate a larger composition region than that of metallic system with only two metal structures (Ni-Nb-Mo). In particular, the predicted GFR of Ni-Nb-Ti system indicated the glass formation composition range of Ni-Nb system as 20-75 at.% Nb, which was close to that of 15-75 at.% Nb predicted in Ni-Nb-Mo system and 15-80 at.% Nb predicted in Ni-Nb-Zr system. The consistency of the glass formation composition range of Ni-Nb system provided further evidence for the reliability of the present simulations.

5. Composition optimization of Ni-Nb-Ti glassy alloys

As discussed in Section 4, the GFR of Ni-Nb-Ti metallic system was derived. If one refers to the GFR, one is able to predict whether glassy alloys can be produced at a chosen composition of the Ni-Nb-Ti system. Nonetheless, other issues that how to access the GFA of ternary Ni-Nb-Ti alloys, and, how to find the optimized compositions for the alloys with large GFA are not solved yet. As mentioned in Section 1, the driving force for amorphization of a crystalline phase can be correlated to the GFA of a particular alloy. From the perspective of thermodynamics, the

formation enthalpy difference between the amorphous glassy alloy and the corresponding crystalline solid solution can be thought as the driving force for amorphization or vitrification, while the formation enthalpy difference between the intermetallic and amorphous alloy could be considered as the resistance for glass formation against crystallization.[54] As intermetallics was difficult to form during the atomic simulations and the formation enthalpy of the intermetallics was also complex to calculate, so the resistance for glass formation wasn't considered for the sake of simplifying the calculation. Besides, the growth of intermetallics is frequently related to the quenching and reheating process of the metallic glasses, which are not involved in present research. As a consequence, the GFA of the Ni-Nb-Ti alloys are able to be assessed based on the driving force for the transformation from crystalline solid solutions to metallic glasses, indicating that the larger the driving forces, the larger the GFA. Furthermore, the optimized compositions can be determined according to the large driving forces of the corresponding alloys.

Suppose that H_{mg} is the average enthalpy (one atom) of the ternary $Ni_xNb_yTi_{100-x-y}$ metallic glass that can be derived from MD simulation and H_{Ni}, H_{Nb}, H_{Ti}, are the enthalpies (one atom) of *fcc*-Ni, *bcc*-Nb and *hcp*-Ti lattices, respectively. The formation enthalpy of metallic glass ΔH^{mg} can be calculated as follows:

$$\Delta H^{mg} = H_{mg} - [x/100 \cdot H_{Ni} + y/100 \cdot H_{Nb} + (100 - x - y)/100 \cdot H_{Ti}], \quad (5)$$

The corresponding formation enthalpy of a crystalline solid solution can be derived from MC simulations. Similar to Equation 5, the formation enthalpy of the $Ni_xNb_yTi_{100-x-y}$ solid solution ΔH^{css} can be calculated as follows:

$$\Delta H^{css} = H_{css} - [x/100 \cdot H_{\mathrm{Ni}} + y/100 \cdot H_{\mathrm{Nb}} + (100 - x - y)/100 \cdot H_{\mathrm{Ti}}], \quad (6)$$

Combing Equations (5) and (6), the formation enthalpy difference between the metallic glass and the corresponding crystalline solid solution ΔH^{dif} can be determined as

$$\Delta H^{dif} = \Delta H^{mg} - \Delta H^{css} = H_{mg} - H_{css}, \quad (7)$$

and ΔH^{dif} is considered as the driving force for a solid solution to vitrify, which can be seen as an indicator of the GFA.

Figure 6 presents the formation enthalpy difference (driving force) and GFA of the Ni-Nb-Ti alloy. The driving forces of more compositions were created through interpolation for visual appeal. From Figure 6, it is noted that ΔH^{dif} is negative within the GFR (region surrounded by red lines), signifying the formation enthalpy of glassy alloy is less than that of the corresponding crystalline solid solution and further, glassy alloys are energetically inclined to form. In addition, the alloys with compositions in red dot region have less ΔH^{dif} than those with other compositions, implying that the driving forces for amorphization and correlated GFA are larger. The red dot composition region is defined as the optimized composition region, within which the metallic glasses have larger GFA and are considered to be more thermally stable. Furthermore, within the optimized composition region, the $Ni_{50}Nb_{35}Ti_{15}$ alloy symbolized by a black pentagram possesses the lowest ΔH^{dif} (–0.5257 eV/atom). So, the maximum driving force for Ni-Nb-Ti alloy to transform to metallic glass is determined at $Ni_{50}Nb_{35}Ti_{15}$ alloy, implying the $Ni_{50}Nb_{35}Ti_{15}$ alloy have the largest GFA. Therefore, the optimum alloy composition of Ni-Nb-Ti metallic glasses can be

defined as $Ni_{50}Nb_{35}Ti_{15}$, signifying that the glassy alloy with the composition of $Ni_{50}Nb_{35}Ti_{15}$ could be more thermally stable and easily attainable than other Ni-Nb-Ti alloys.

To verify the validity of the evaluated GFA, the GFA revealed by atomic simulations were compared with experimental observations. Junpei Sakurai et al.[13] discovered that the composition region of the amorphous alloy with a high heat resistance was Ni: 40-75, Nb: 10-50, and Ti 0-30 at.%, which overlaps a large part of the optimized composition region shown in Figure 6. The metallic glasses with the compositions in the optimized composition region have large GFA, indicating high thermal stability, which corresponds to the high heat resistance revealed by experiment data in Ref. 13. The good agreement has corroborated that the prediction of the optimized compositions with large GFA in this simulation is reasonable and valid. Besides, Junpei et al.[13] also found that the $Ni_{56}Nb_{33}Ti_{11}$ and $Ni_{49}Nb_{35}Ti_{16}$ alloys possess high heat and corrosion resistances and good mechanical properties. Wei Zhang et al.[12] discovered that the $Ni_{60}Nb_{25}Ti_{15}$ bulk glassy alloy exhibited high thermal stability and excellent mechanical properties with high compressive fracture strength. All the three alloy compositions above are located within the optimized composition region suggests that the optimized compositions could offer helpful reference for searching for alloys with good physical, chemical or mechanical properties.

In the discussion above, the driving force or formation enthalpy difference has been correlated to the readiness of glass forming, i.e. GFA. This deduction has been

applied in several alloy systems such as Ni-Nb-Mo[29] and Ni-Nb-Zr[53] systems, which could offer reference to the calculation of driving force in present research. It is seen that all the optimized composition region (red dot region) of the three Ni-Nb-based systems are located close to the Ni-Nb side and further, the prime elements of the optimized compositions are Ni and Nb. Nevertheless, the optimized composition regions of the three systems are located in different areas, in which the evaluated driving forces exhibit some distinctions. The maximum driving forces of Ni-Nb-Mo or Ni-Nb-Zr alloys are in the range from –0.4 to –0.5 eV/atom, which is in accordance with the maximum driving force (–0.5257 eV/atom) in Ni-Nb-Ti system. The consistency implies that the calculation of the driving force of Ni-Nb-Ti alloy is reasonable and reliable. However, it should be noted that the GFA evaluation of Ni-Nb-Ti alloys with three different structures (*fcc*, *bcc* and *hcp*) has shown precise consistency with the experimental observations, which reveals some distinctions from the previous research.

To illustrate the variation of driving force more clearly, two profiles were selected, i.e. line FG ($Ni_{50}Nb_xTi_{50-x}$ alloys, x = 0-50) and line HI ($Ni_{60}Nb_yTi_{40-y}$ alloys, y = 0-40) as shown in Figure 6. The driving forces of the two series of alloys for amorphization were shown in Figure 7. All the driving forces of the $Ni_{50}Nb_xTi_{50-x}$ alloys are negative, indicating that the $Ni_{50}Nb_xTi_{50-x}$ metallic glasses are inclined to form. Moreover, the driving forces of the $Ni_{50}Nb_xTi_{50-x}$ alloys first increased and then reduced, implying a maximum driving force at the composition of $Ni_{50}Nb_{35}Ti_{15}$. The variation of the driving forces reveals that the $Ni_{50}Nb_{35}Ti_{15}$ alloy has the largest

driving force among the $Ni_{50}Nb_xTi_{50-x}$ alloys, meaning the $Ni_{50}Nb_{35}Ti_{15}$ metallic glass has the largest GFA and is more energetically stable than other $Ni_{50}Nb_xTi_{50-x}$ metallic glasses. From the inset in Figure 5, one can find that the driving forces of $Ni_{60}Nb_yTi_{40-y}$ alloys show similar variation tendency as those of $Ni_{50}Nb_xTi_{50-x}$ alloys, manifesting that the $Ni_{60}Nb_{25}Ti_{15}$ metallic glasses possess the largest driving force among the $Ni_{60}Nb_yTi_{40-y}$ alloys. As a consequence, the $Ni_{60}Nb_{25}Ti_{15}$ metallic glass possesses larger GFA and is more easily attainable than other $Ni_{60}Nb_yTi_{40-y}$ metallic glasses, revealing excellent consistency with the fact that the largest attainable size of the bulk glassy alloy was 1.5 mm for $Ni_{60}Nb_{25}Ti_{15}$ alloy among all the $Ni_{60}Nb_yTi_{40-y}$ alloys.[12] The excellent consistency between simulation results with experiment observations provides further evidence for the validity of the atomic simulation results.

From the discussion above, the GFAs of Ni-Nb-Ti alloys were evaluated based on the driving force for amorphization through atomic simulations. According to the predicted GFAs, the optimized composition region within which the alloys have larger GFAs was designed and furthermore, the optimum composition was pinpointed at $Ni_{50}Nb_{35}Ti_{15}$. The compositions predicted and optimized by atomic simulations have been corroborated to be reasonable and valid through comparing with experiment data.

7. Concluding remarks

A long range realistic potential (LREP) of Ni-Nb-Ti system was first constructed, and hereby utilized in MD simulation to investigate the formation of Ni-Nb-Ti glassy alloys. The atomic simulations uncover the atomic process that crystalline solid solutions evolved to glassy alloys, and derive a quantitative pentagon Ni-Nb-Ti glass formation region (GFR) within which amorphous alloys are inclined to form. The formation enthalpy difference between the glassy alloy and corresponding crystalline solid solution was thought as the driving force for amorphization, which could be correlated to the glass-forming ability (GFA) of the alloy. According to the GFA of alloys, the optimized composition region within which metallic glasses have larger GFAs or are more thermally stable were optimized and furthermore, the optimum composition with the largest GFA was determined at $Ni_{50}Nb_{35}Ti_{15}$. The compositions predicted and optimized by atomic simulations have been certified to be reasonable and valid through comparing with observations in experiment and simulation results of other similar alloys, offering guidance to design the optimized compositions of Ni-Nb-Ti metallic glasses with desired GFA.

Acknowledgements

The authors greatly appreciate the financial assistance from the National Natural Science Foundation of China (51131003), the Ministry of Science and Technology of China (973 Program 2011CB606301, 2012CB825700) and the Administration of Tsinghua University.

References:

1 A. Inoue, *Acta Mater.*, 2000, **48**, 279-306.

2 W. L. Johnson, *Mrs Bull.*, 1999, **24**, 42-56.

3 A. L. Greer, *Science*, 1995, **267**, 1947-1953.

4 L. Tian, Y. Cheng, Z. Shan, J. Li, C. Wang, X. Han, J. Sun, and E. Ma, *Nat. Commun.*, 2012, **3**, 609.

5 Q. Zeng, H. Sheng, Y. Ding, L. Wang, W. Yang, J. Jiang, W. L. Mao, and H. Mao, *Science*, 2011, **332**, 1404-1406.

6 J. C. Ye, J. Lu, C. T. Liu, Q. Wang, and Y. Yang, *Nat. Mater.*, 2010, **9**, 619-623.

7 A. Inoue and B. Shen, *Formation and Applications of Bulk Glassy Alloys in Late Transition Metal Base System*. 2006.

8 A. Inoue, B. Shen and A. Takeuchi, *Mater. Trans.*, 2006, **47**, 1275.

9 T. Nagase, M. Ueda and Y. Umakoshi, *J. Alloy. Compd*, 2009, **485**, 304-312.

10 L. Y. Chen, Z. D. Fu, W. Zeng, G. Q. Zhang, Y. W. Zeng, G. L. Xu, S. L. Zhang, and J. Z. Jiang, *J. Alloy. Compd*, 2007, **443**, 105-108.

11 S. Jayalakshmi, V. S. Vasantha, E. Fleury, and M. Gupta, *Appl. Energ.*, 2012, **90**, 94-99.

12 Z. Wei and A. Inoue, *Mater. Trans.*, 2002, **43**, 2342-2345.

13 J. Sakurai, H. Kozako, N. Mukai, Y. Ohnuma, T. Takahashi, and S. Hata, *J. J. Appl. Phys.*, 2011, **50**, 8720181.

14 W. Cai, X. L. Meng and L. C. Zhao, *Curr. Opin. Solid St. M.*, 2005, **9**, 296-302.

15 F. Yongqing, D. Hejun, H. Weimin, Z. Sam, and H. *Min, Sens. and Actuat. A*,

2004, **A112**, 395-408.

16 W. H. Wang, C. Dong and C. H. Shek, *Mater. Sci. Eng. R*, 2004, **44**, 45-89.

17 Z. P. Lu, H. Bei and C. T. Liu, *Intermetallics*, 2007, **15**, 618-624.

18 D. Turnbull, J. Phys. Colloq., 1974, **35**, C1-C4.

19 T. Egami and Y. Waseda, *J. Non-Cryst. Solids*, 1984, **64**, 113-134.

20 A. Inoue, *Bulk Amorphous Alloys-Preparation and Fundamental Characteristics Materials Science Foundations 4*. 1998, Trans Tech Publications, Netherlands.

21 J. H. Li, Y. Dai, Y. Y. Cui, and B. X. Liu, *Mater. Sci. Eng. R*, 2011, **72**, 1-28.

22 K. Zhang, M. Wang, S. Papanikolaou, Y. Liu, J. Schroers, M. D. Shattuck, O. Apos, and C. S. Hern, J. Chem. Phys., 2013, **139**, 12453.

23 J. H. Li, Y. Dai and X. D. Dai, *Intermetallics*, 2012, **31**, 292-320.

24 B. X. Liu, W. S. Lai and Q. Zhang, *Mater. Sci. Eng. R*, 2000, **29**, 1-48.

25 J. H. Li, S. Z. Zhao, Y. Dai, Y. Y. Cui, and B. X. Liu, *J. Appl. Phys.*, 2011, **109**, 113538.

26 H. W. Sheng, G. Wilde and E. Ma, *Acta Mater.*, 2002, **50**, 475-488.

27 J. H. Li, Y. Dai, X. D. Dai, T. L. Wang, and B. X. Liu, *Comp. Mater. Sci.*, 2008, **43**, 1207-1215.

28 Y. Dai, J. H. Li, X. L. Che, and B. X. Liu, J. Phys. Chem. B, 2009, **113**, 7282-7290.

29 Y. Li, S. Y. Luo, J. H. Li, J. B. Liu, and B. X. Liu, *J. Mater. Sci.*, 2014, **49**, 7263-7272.

30 X. D. Dai, Y. Kong and J. H. Li, *Phys. Rev. B*, 2007, **75**, 104101.

31 X. D. Dai, J. H. Li and Y. Kong, *Phys. Rev. B*, 2007, **75**, 52102.

32 Y. Dai, J. H. Li and B. X. Liu, *J. Phys.-Condens. Mat.*, 2009, **21**

33 M. I. Baskes and B. Lee, *Phys. Rev. B*, 2000, **62**, 8564-8567.

34 M. D. Segall, P. J. Lindan, M. J. Probert, C. J. Pickard, P. J. Hasnip, S. J. Clark, and M. C. Payne, *J. Phys.-Condens. Mat.*, 2002, **14**, 2717.

35 S. J. Clark, M. D. Segall, C. J. Pickard, P. J. Hasnip, M. I. Probert, K. Refson, and M. C. Payne, Z. Kristallog., 2005, **220**, 567-570.

36 J. P. Perdew and Y. Wang, *Phys. Rev. B*, 1992, **45**, 13244.

37 C. Kittel, *Introduction to solid state physics*. 1996, Wiley New York.

38 G. Simmons and H. Wang, *Single crystal elastic constants and calculated aggregate properties: A handbook 2nd ed.* 1971, MIT Press, Cambridge.

39 W. M. Haynes, D. R. Lide and T. J. Bruno, *CRC Handbook of Chemistry and Physics 2012-2013*. 2012, CRC press.

40 P. Villars, *Pearson's Handbook Desk Edition: Crystallographic Data for Intermetallic Phases*. 1997, ASM International Materials Park, OH.

41 J. H. Rose, J. R. Smith, F. Guinea, and J. Ferrante, *Phys. Rev. B*, 1984, **29**, 2963.

42 See http://lammps.sandia.gov for LAMMPS package

43 S. Y. Luo, J. H. Li, Y. Y. Cui, Y. Dai, and B. X. Liu, *Intermetallics*, 2012, **25**, 109-114.

44 A. Z. Panagiotopoulos, N. Quirke, M. Stapleton, and D. J. Tildesley, *Mol. Phys.*, 1988, **63**, 527-545.

45 Y. Dai, J. H. Li, X. L. Che, and B. X. Liu, *J. Mater. Res.*, 2009, **24**, 1815-1819.

46 Y. Q. Cheng and E. Ma, *Prog. Mater. Sci.*, 2011, **56**, 379-473.

47 E. Sváb, G. Mészáros, G. Konczos, S. N. Ishmaev, S. L. Isakov, I. P. Sadikov, and A. A. Chernyshov, *J. Non-Cryst. Solids*, 1988, **104**, 291-299.

48 T. Fukunaga, N. Watanabe and K. Suzuki, *J. Non-Cryst. Solids*, 1984, **61 – 62, Part 1**, 343-348.

49 Z. J. Zhang, H. Y. Bai, Q. L. Qiu, T. Yang, K. Tao, and B. X. Liu, *J. Appl. Phys.*, 1993, **73**, 1702-1710.

50 H. Kimura, A. Inoue, S. Yamaura, K. Sasamori, M. Nishida, Y. Shinpo, and H. Okouchi, *Mater. Trans.*, 2003, **44**, 1167-1171.

51 A. I. Oreshkin, V. N. Mantsevich, S. V. Savinov, S. I. Oreshkin, V. I. Panov, A. R. Yavari, D. B. Miracle, and D. V. Louzguine-Luzgin, *Acta Mater.*, 2013, **61**, 5216-5222.

52 R. B. SCHWARZ, R. R. PETRICH and C. K. SAW, *J. Non-Cryst. Solids*, 1985, **76**, 281-302.

53 S. Y. Luo, J. H. Li, J. B. Liu, and B. X. Liu, *Acta Mater.*, 2014, **76**, 482-492.

54 L. Xia, W. H. Li, S. S. Fang, B. C. Wei, and Y. D. Dong, *J. Appl. Phys.*, 2006, **99**, 261032.

Tables

Table 1. The six sets of constructed LREP parameters for Ni-Nb-Ti system

	Ni	Nb	Ti	Ni-Nb	Ni-Ti	Nb-Ti
m	4	4	4	4	4	4
n	5	8	4	6	5	6
r_{c1} (Å)	5.768881	4.802790	5.795909	5.333995	4.420312	5.241036
r_{c2} (Å)	7.245217	6.818734	6.957239	5.041915	7.818882	6.880792
c_0 (10^{-19} J)	0.452613	16.724606	0.549500	5.984657	2.450642	2.227142
c_1 (10^{-19} J/Å^{m+1})	-0.550598	-22.895200	-0.623598	-7.564475	-2.652920	-3.162071
c_2 (10^{-19} J/Å^{m+2})	0.249231	11.810592	0.273602	3.592397	1.159837	1.746392
c_3 (10^{-19} J/Å^{m+3})	-0.049850	-2.696127	-0.054871	-0.752354	-0.261233	-0.434629
c_4 (10^{-19} J/Å^{m+4})	0.003751	0.228753	0.004280	0.057993	0.029584	0.040796
α (10^{-19} J/Å^{n})	0.002146	0.000473	0.032226	0.125790	0.005924	0.004534

Table 2. Physical properties (Lattice constants (*a*, *c* Å), Cohesive energies (E_c, eV), Bulk modulus (B_0, Mbar), Elastic constants (C_{ij}, Mbar)) of *hcp*-Ti obtained from the LREP (first line) and the experimental data (second line)[33-35].

hcp-Ti	*a*	*c*	E_c	C_{11}	C_{12}	C_{13}	C_{33}	C_{44}	B_0
fitted	2.946	4.681	4.845	1.647	0.729	0.683	1.863	0.412	1.039
exprt	2.95	4.68	4.85	1.624	0.92	0.69	1.807	0.467	1.05

Table 3. Physical properties of the Ni-Nb intermetallics obtained from the LREP (first line) and those from *ab initio* calculations (second line). [36-38]

	Nb_3Ni		NbNi	$NbNi_3$	
	$L1_2$	$D0_{19}$	B2	$L1_2$	$D0_{19}$
a or *a*, *c* or *a*,	3.864	5.433,4.661	3.165	3.721	5.213,4.395
b, *c* (Å)	4.05	5.655,4.765	3.095	3.70	5.151,4.342
E_c (eV)	6.546	6.597	6.110	5.443	5.427
	6.707	6.648	6.047	5.439	5.478
B_0 (Mbar)	1.466	1.304	2.205	1.892	2.175
	1.765	1.513	2.166	1.898	2.123

Table 4. Physical properties of the Ni-Ti intermetallics obtained from the LREP (first line) and those from *ab initio* calculations (second line) or experiment data (indicated by asterisk)[32].

	Ni_3Ti		NiTi	$NiTi_2$	$NiTi_3$
	$L1_2$	$D0_{24}$	B2	$E9_3$	$L1_2$
a or *a*, *c*	3.578	5.052,8.339	2.933	11.139	3.833
(Å)	3.618	5.101, 8.307*	3.007*	11.293*	3.936
E_c (eV)	5.182	5.175	4.932	5.079	4.839
	5.080	5.095	5.062	5.039	4.868
B_0 (Mbar)	1.939	1.855	1.528	1.260	1.205
	1.941	1.882	1.618	1.418	1.281

Table 5. Physical properties of the Nb-Ti intermetallics obtained from the LREP (first line) and those from *ab initio* calculations (second line).

	Nb_3Ti	NbTi	$NbTi_3$
	$L1_2$	B2	$L1_2$
a (Å)	4.141	3.278	4.160
	4.183	3.263	4.123
E_c (eV)	6.665	6.117	5.463
	6.666	6.135	5.446
B_0 (Mbar)	1.299	1.379	1.261
	1.346	1.365	1.236

Figure captions

Figure 1 The partial pair correlation functions $g_{AB}(r)$ of simulated (a) $Ni_{62}Nb_{38}$ alloy and (b) $Ni_{40}Ti_{60}$ alloy, respectively.

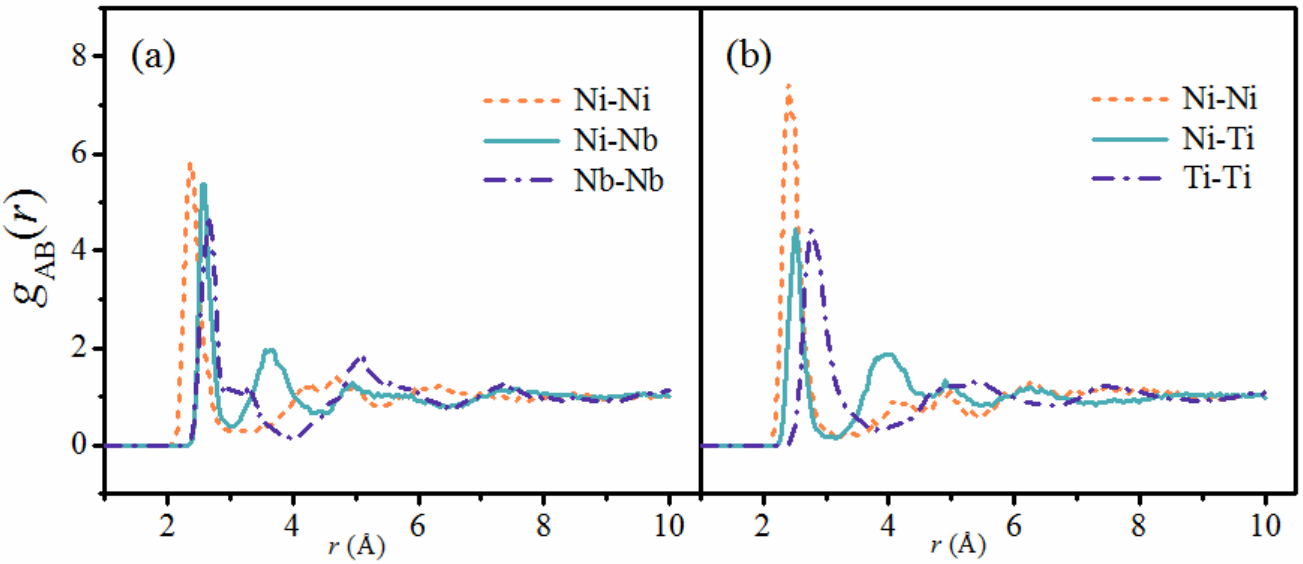

Figure 2. The $g(r)$ and atomic projections for (a), (b) crystalline structure ($Ni_{15}Nb_{45}Ti_{40}$), (c), (d) amorphous structure ($Ni_{25}Nb_{40}Ti_{35}$), respectively.

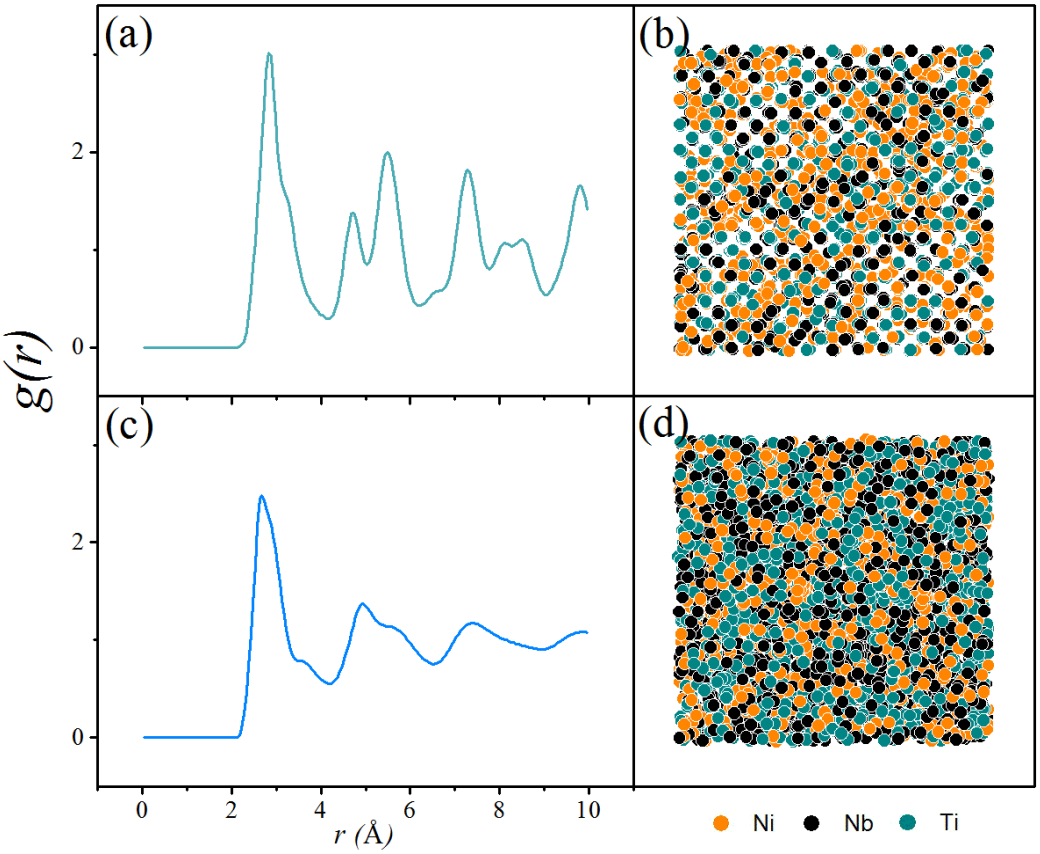

Figure 3. The distribution of coordination number (a) and Voronoi volume (b) for crystalline $Ni_{15}Nb_{45}Ti_{40}$ alloy (cyan) and amorphous $Ni_{25}Nb_{40}Ti_{35}$ alloy (orange).

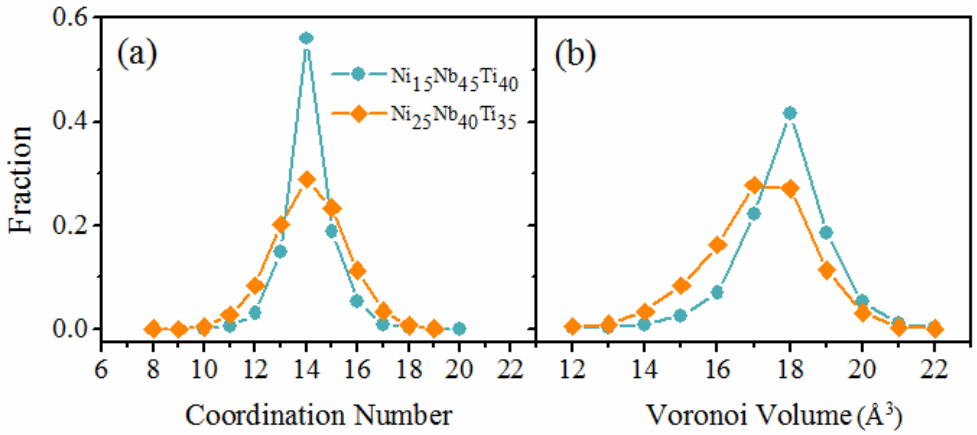

Figure 4. Fraction of the most common Voronoi polyhedra for (a) crystalline $Ni_{15}Nb_{45}Ti_{40}$ alloy, (b) amorphous $Ni_{25}Nb_{40}Ti_{35}$ alloy, respectively.

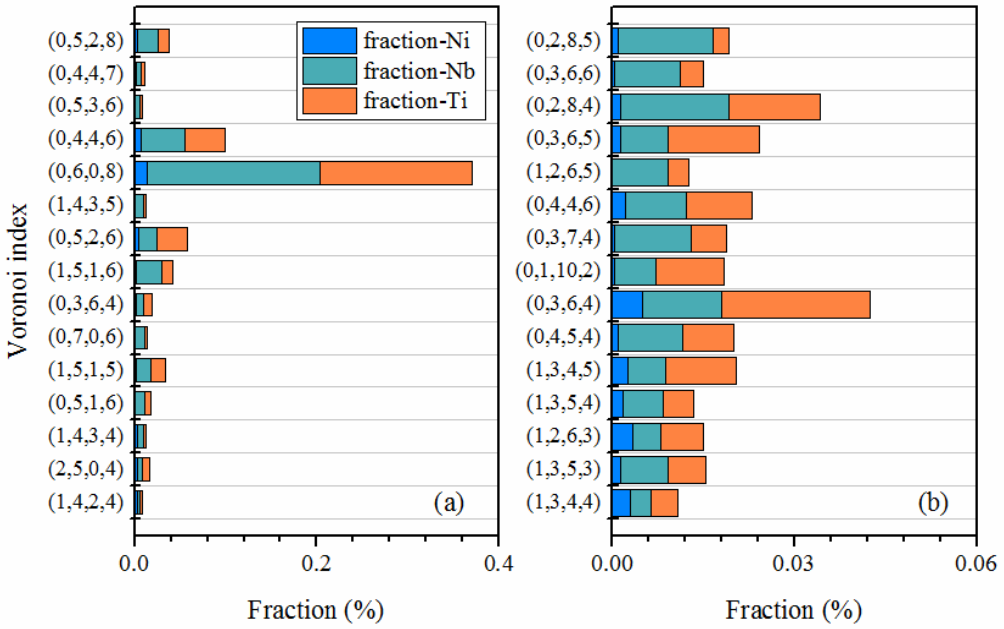

Figure 5. The GFR (shaded zone) obtained from atomic simulations with experimental results (green triangles for IBM, red hexagons for RS, orange rhombuses for CAPD, and blue inverted triangles for MA) for the Ni-Nb-Ti system.

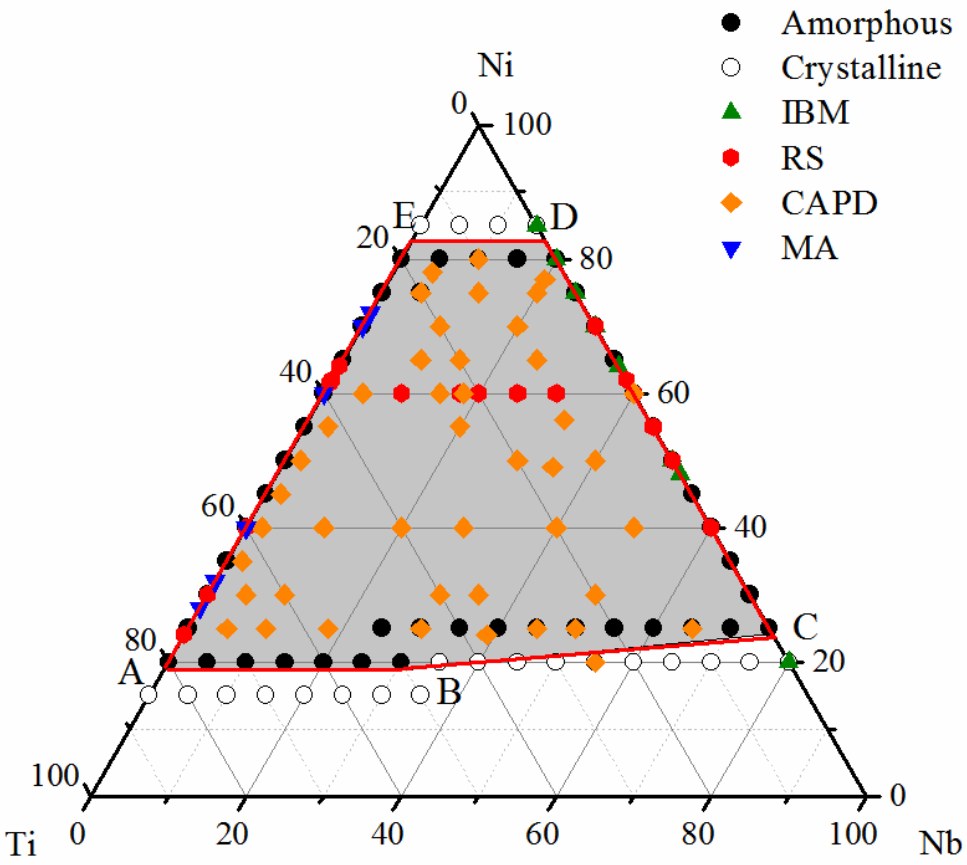

Figure 6. The formation enthalpy difference (eV/atom) between the metallic glass and its corresponding solid solution of Ni-Nb-Ti system. The black pentagram indicates the optimum composition with the largest GFA.

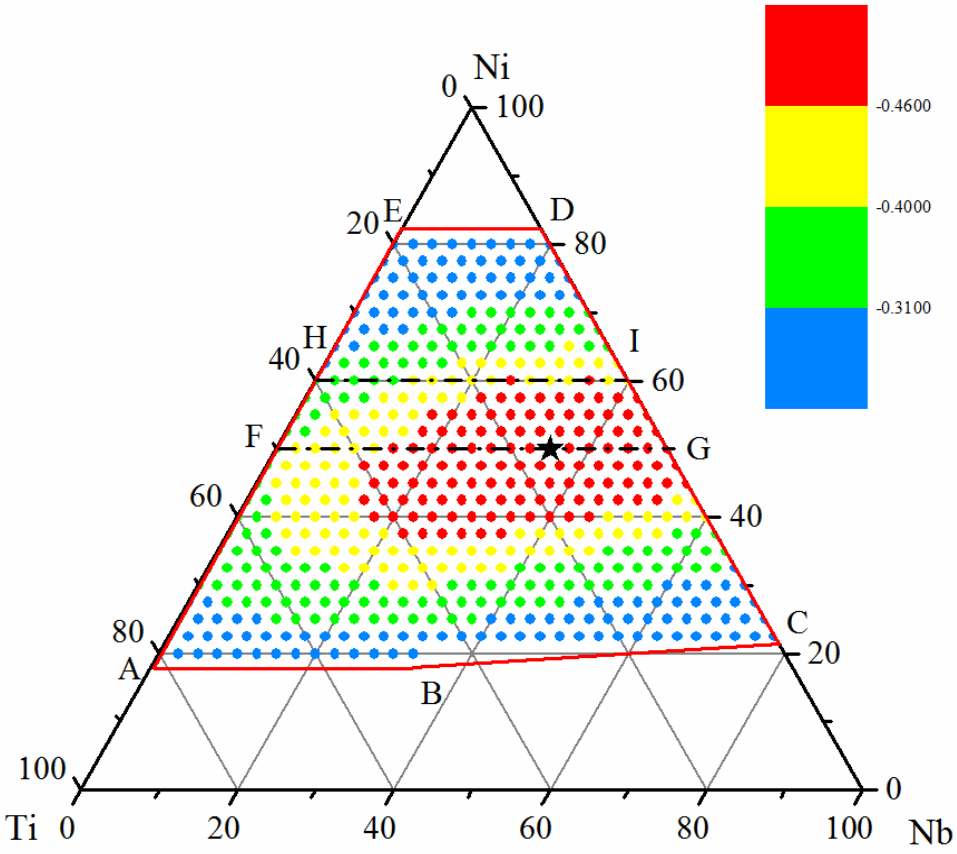

Figure 7. The driving forces of the $Ni_{50}Nb_xTi_{50-x}$ alloys for amorphization. (Inset: driving forces of $Ni_{60}Nb_yTi_{40-y}$ alloys for amorphization).

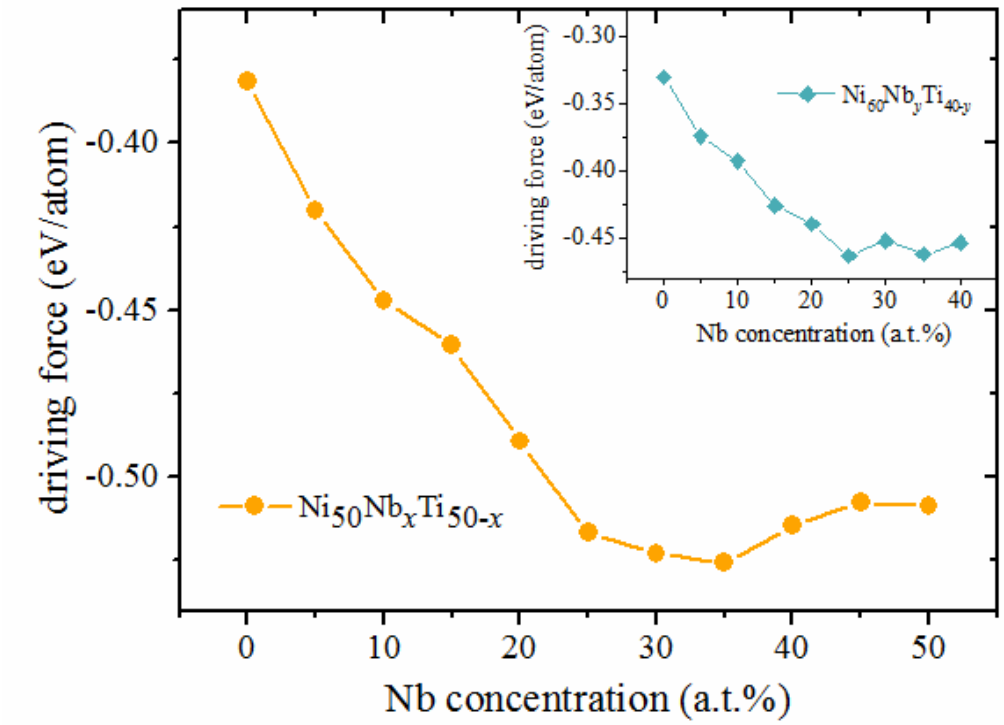

Graphic:

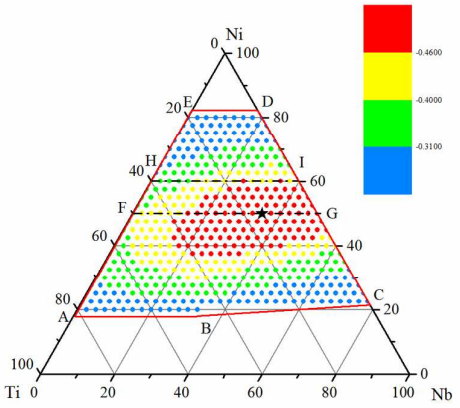

Highlights:

The optimized composition region and the optimum composition with the largest GFA were obtained through atomic simulations.